Algorithmic climate change functions for the use in eco-efficient flight planning

van Manen, J.; Grewe, V.

DOI
10.1016/j.trd.2018.12.016

Publication date
2019

Document Version
Final published version

Published in
Transportation Research Part D: Transport and Environment

Transportation Research Part D 67 (2019) 388–405

Contents lists available at ScienceDirect

Transportation Research Part D

journal homepage: www.elsevier.com/locate/trd

Algorithmic climate change functions for the use in eco-efficient flight planning

J. van Manen[a], V. Grewe[a,b,*]

[a] Delft University of Technology, Faculty of Aerospace Engineering, Section Aircraft Noise and Climate Effects, Netherlands
[b] Deutsches Zentrum für Luft- und Raumfahrt, Institut für Physik der Atmosphäre, Oberpfaffenhofen, Germany

ARTICLE INFO

Keywords:
Aviation
Climate impact
Meteorology
Algorithm
Regression analysis

ABSTRACT

Aviation contributes significantly to anthropogenic climate change, and one promising possibility for mitigation is eco-efficient flight planning by avoiding climate sensitive regions with only small changes in the aircraft trajectories. Climate sensitive regions result from strong spatial variation of the global climate impact of local non-CO_2 emissions, which are expressed by so-called climate change functions. Previous research established high-fidelity climate change functions (CCFs) for aviation water vapour and NO_x emissions, and contrail formation with a climate model as inputs for air traffic optimisation. The mitigation potential in this case study is promising but the climate change function simulations are too computationally intensive for real-time calculation and thus cannot be applied operationally. In this study we show for the first time that this problem can be overcome by formulating algorithmic approximations of the global climate impact. Here we approximate water vapour concentration changes from local aviation water vapour emissions, ozone changes from local NO_x emissions and methane changes from local NO_x emissions (i.e. algorithmic climate change functions; aCCFs) from instantaneous model weather data using regression analysis. Four candidate algorithms are formulated per chemical species and traded off. The final adjusted regression coefficients, indicating how well the aCCFs represent the CCFs, are 0.59, 0.42, and 0.17 for water vapour, ozone and methane. The results show that the meteorology at the time of emission largely controls the fate of the emitted species, where the quality of the aCCF degrades with increasing lifetime of the respective species.

1. Introduction

The importance of reducing anthropogenic climate change is well-recognised, especially since the signing of the Paris Agreement of the United Nations Framework Convention on Climate Change (UNFCCC), which aims to strengthen the global response to the threat of climate change by keeping a global temperature rise this century well below 2 °C above pre-industrial levels and to pursue efforts to limit the temperature increase even further to 1.5 °C. The share of aviation in anthropogenic radiative forcing (RF) in 2005 was about 3.5% and is expected to grow to 4–4.7% by mid-century (excluding contrail-induced cirrus effects, Lee et al., 2009). This share is estimated to be around 5% in 2005 (Lee et al., 2009, and updates in Grewe et al., 2017a), when contrail cirrus effects are included. Aviation induced radiative forcing and as a result long-term climate change is caused by emissions of carbon dioxide (CO_2), nitrogen oxides (NO_x), water vapour (H_2O), carbon, sulphur dioxide (SO_2), sulphur and carbon aerosols, and through the formation of contrails (Lee et al., 2010).

* Corresponding author at: Delft University of Technology, Faculty of Aerospace Engineering, Section Aircraft Noise and Climate Effects, Netherlands.
E-mail address: Volker.Grewe@dlr.de (V. Grewe).

https://doi.org/10.1016/j.trd.2018.12.016

Water vapour emissions directly lead to radiative forcing through increased water vapour concentrations in the atmosphere. The lifetime of emitted water vapour depends strongly on altitude and varies between hours and months (Lee et al., 2010). Wilcox et al. (2012) found 0.86 [0.34–1.34] mW m^{-2} annual global-mean adjusted RF from 2006 aviation water vapour emissions.

Emitted NO_x has a negligible direct climate impact but leads to a short-term increase in ozone production rates (thus positive radiative forcing) and a long-term increase in methane oxidation (thus negative radiative forcing). Significant seasonal and spatial variability exists in the size and lifetime of perturbations caused by NO_x emissions, mainly due to differing background chemical concentrations and insolation (Stevenson et al., 2004; Köhler et al., 2008; Stevenson and Derwent, 2009; Köhler et al., 2013). The annual-mean global-mean adjusted RF from aviation NO_x emissions in 2005 was about 13.8 [3.8–15.7] mW m^{-2}, 26.3 [8.4–82.3] mW m^{-2} from ozone production and −12.5 [−76.2 to −2.1] mW m^{-2} from methane oxidation (Lee et al., 2009), assuming 100% anticorrelation between both effects. Holmes et al. (2011) found 79% anticorrelation between both effects and Lee et al. (2010) showed that the ratio of the RFs (RF of ozone divided by the RF of methane) is −1.65 with a standard variability of 21% and agree well with newer findings (Pitari et al., 2017). Both studies agree well and show that the confidence range for NO_x is likely too conservative.

A number of different strategies are being pursued to reduce the climate impact of aviation, e.g. increasing fuel efficiency, low NO_x engines, the use of alternative fuels, including the development of hydrogen fuels. For mitigation of non-CO_2 climate impacts, a promising development is eco-efficient flight planning, because the effects of non-CO_2 emissions show strong spatiotemporal variations (Lee et al., 2010). Current aircraft routes are optimised for time and costs which are related to fuel burn and CO_2 climate impact, and efforts to reduce the total climate impact will lead to a cost trade-off.

Previous work on climate-optimal flight routes (e.g. Sridhar et al., 2013; Schumann et al., 2011; Hartjes et al., 2016; Zou et al., 2016) has largely focused on reducing the climate impact of contrails (for details see Table 1). Some studies include other non-CO_2 effects (e.g. NO_x-climate effects), but on a climatological basis, not taking into account altitude or weather effects (e.g., Rosenow et al., 2017).

To enable a case study of the mitigation potential of climate-optimised air traffic over the North Atlantic as part of the EU project REACT4C (Reducing Emissions from Aviation by Changing Trajectories for the benefit of Climate; http://www.react4c.eu/), Grewe et al. (2014b) developed climate change functions (CCFs, i.e. the spatiotemporal variation of global-average climate impact from a local emission) for carbon dioxide, nitrogen oxides, water vapour and contrails using a state-of-the-art climate model, as an input for the air traffic optimisation. These CCFs are used to describe “climate-sensitive regions”. These regions describe time-varying 3D areas of the atmosphere, where emissions from aviation contribute significantly larger to climate change than in other regions. Note that this represents an integral view on the aviation effects, from the emission through atmospheric concentration changes and radiation budgets to eventually mean near-surface temperature changes. Hence individual aspects, such as areas where contrails are formed are an integral part of this approach. The full set of CCFs for eight weather patterns is described by Frömming et al. (2019). Results of the air traffic optimisation (Grewe et al., 2017b) show a 10% reduction in climate impact for a 1% cost increase, but the calculations of CCFs and the optimisation are very computationally intensive. For future implementation, real-time results are desired whereby approximate CCFs could be calculated in-line with operational aviation-weather prediction. Matthes et al. (2017) present an outline of the approach taken in the EU project ATM4E (Air Traffic Management for Environment; http://www.atm4e.eu/), including development and verification of contrail, water vapour and nitrogen oxides CCF approximations. That approach also includes other environmental effects such as local air quality and noise, which could potentially act in opposing directions (Mahashabde et al., 2011).

Here, we investigate the spatial and temporal variability of the simulated REACT4C CCFs for water vapour and NO_x emissions and formulate predictive algorithms based on instantaneous weather data from the climate model used to simulate the CCFs. The results we present facilitates real-time calculation of CCFs in a numerical weather prediction routine and fits into the approach presented by Matthes et al. (2017). These algorithms can easily be used for air traffic optimisations, either to estimate climate impact of individual aircraft trajectories or to optimise air traffic with respect to its climate impact. It hence comprises a large advancement compared to global or regional climate impact estimates (e.g., Rosenow et al., 2017).

An overview of the methods of the previous REACT4C work and this work is given in Section 2. Algorithms for water vapour and NO_x emissions are given in Sections 3 and 4, respectively. Comparisons between the high-fidelity, simulated CCFs and the algorithmic approximations are provided in Section 5, followed by a summary and discussion of the results.

Table 1
Previous studies on climate optimised routing showing the principle differences in implementation.

Source	Climate variable	Climate metric	Routing flexibility
Schumann et al. (2011)	Contrails, CO_2	RF/Energy Forcing taking into account weather conditions	Vertical
Sridhar et al. (2013)	Contrails, CO_2	Temperature change based on mean contrail properties	Vertical and horizontal
Hartjes et al. (2016)	Contrails, CO_2	Contrail occurrence/RF based on mean contrail properties	3D
Zou et al. (2016)	Contrails, CO_2	GWP with mean contrail properties for night and day formation	4D
Rosenow et al. (2017)	NO_x, CO_2	GWP, with regional varying GWP for NO_x, and a globally constant CO_2 offset for all other non-CO_2 effects	3D
Grewe et al. (2014b,a, 2017b)	Contrails, CO_2, NO_x, H_2O	Mean temperature change varying with emission location die to meteorology	3D

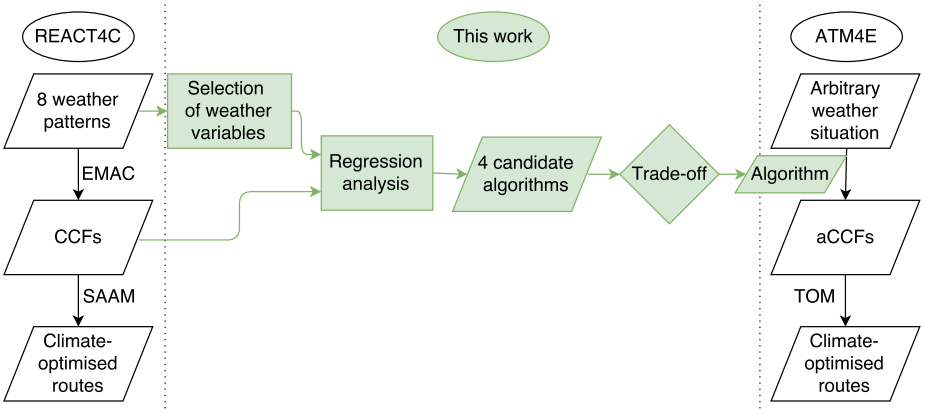

Fig. 1. Sketch of methods used in this work (green) and relationship to the EU research projects REACT4C and ATM4E. Note that results of REACT4C (left) are basically input to this work and that further results of ATM4E (right side) are given for motivation only and are not further covered in this work. This approach is followed three times: for aviation water vapour, ozone and methane effects. SAAM and TOM are trajectory models, see Grewe et al. (2014b) and Matthes et al. (2017). (For interpretation of the references to colour in this figure legend, the reader is referred to the web version of this article.)

2. Model, data and method

In this section the relevant methods are explained chronologically, as they were developed either previously within REACT4C (Sections 2.2 and 2.3) or developed within this work (Section 2.4): the choice of weather patterns to simulate CCFs for, the base model and specific approach for simulating the CCFs, and the algorithm formulation specific to this work. Fig. 1 shows how this work fits into the framework of the EU research projects REACT4C and ATM4E. Weather data and CCF data are provided from results of the REACT4C project (left part) and the objective is to formulate algorithms (green box) for application in the ATM4E project. Note that contrail aCCFs will be developed elsewhere and that also no algorithm is necessary for the emission of CO_2, because the long lifetimes of CO_2 lead to a uniform mixing in the atmosphere and this value is available from ATM4E.

Section 2.1 details the eight REACT4C weather patterns, and Sections 2.2 and 2.3 explain the EMAC model and CCF calculation. Section 2.4 expands on the green blocks in Fig. 1, which explain the processes between REACT4C data and algorithmic results. On the right side of Fig. 1 one possible application of our algorithmic climate change functions is given, in order to motivate the application of our findings. This indicates one important feature: the applicability to any arbitrary weather situation. More details on the REACT4C and ATM4E methods are provided by Grewe et al. (2014b) and Matthes et al. (2017), respectively.

2.1. Weather patterns

CCFs are simulated for emissions during eight model days that represent the eight weather patterns presented by Irvine et al. (2013) for cruise altitude over the North Atlantic. In this method 21 years of winter and summer meteorological re-analysis data are analysed by projecting the geopotential height anomaly of each day onto two distinct teleconnection patterns, the North Atlantic Oscillation and the East Atlantic. This produces five patterns for winter (WP1–5) and three for summer (SP1–3), with distinct position and strength of the jet stream and thus also distinct cost-optimal aircraft routes in both directions from which climate-optimal routes are likely to deviate. The winter patterns WP1 to WP5 occur 19, 19, 17, 17, and 29% of the days within the 21 seasons, respectively, and the summer patterns SP1 to SP3 occur around 20, 20, and 60% of the days (Irvine et al., 2013).

2.2. Base model

The ECHAM/MESSy Atmospheric Chemistry (EMAC) model is a numerical chemistry and climate simulation system that includes sub-models describing tropospheric and middle atmosphere processes and their interaction with oceans, land and human influences (Jöckel et al., 2010). The second version of the Modular Earth Submodel System (MESSy2) is used to link the individual physical and chemical processes described in submodels. Here EMAC (version 2.42) is applied in the T42L41 resolution, i.e. with a spherical truncation of T42 (corresponding to a quadratic Gaussian grid of approximately $2.8^\circ \times 2.8^\circ$ in latitude and longitude) with 41 vertical hybrid pressure levels from the surface to an upper layer centred at 5 hPa. The core atmospheric model is the fifth generation European Centre Hamburg general circulation model (ECHAM5, Roeckner et al., 2006) and the chemistry is modelled by MECCA (version 3.2, Sander et al., 2011). The submodels AIRTRAC and CONTRAIL are specifically developed for calculating CCFs (Grewe et al., 2014b).

2.3. Climate change functions

Emissions are released on a grid of six longitudes (315–360°E), seven latitudes (30–80°N), and four pressure altitudes (200–400 hPa) at 12 UTC resulting in 168 positions per weather pattern. Only for WP1 two additional time coordinates were simulated (Grewe et al., 2014b) which are not used for this work.

The tagging approach developed by Grewe (2013) is used and adapted so that emissions do not feed into model background concentrations, but allow for tracking of atmospheric changes. To facilitate the tagging approach, the Lagrangian submodel ATTILA is used to transport the emitted species in air parcels. A unit emission of NO and water vapour is released at each position, which is split into 50 air parcels that are randomly distributed over the corresponding EMAC gridbox.

When precipitation occurs in the background EMAC gridbox, a proportional amount of water vapour rains out of the tracked air parcels in that gridbox. A detailed non-methane hydrocarbon chemistry is computed in the background and chemical production and loss rates as well as reaction rate constants are provided to the AIRTRAC submodel to keep track of the development of ozone and methane contributions from a NO_x emission by a simplified tagging scheme. After emission, additional NO_x enhances the reaction between HO_2 and NO which forms NO_2 and OH. NO_2 easily photolyses to form $O(^3P)$ which forms ozone. Note that ozone and HO_2 compete in the reaction with NO and the reaction between NO and that HO_2 leads to an ozone increase, whereas the reaction between NO and ozone is effectively a null cycle. The increased ozone from aviation NO_x emissions is also destroyed by reacting with OH and HO_2. The emitted NO_x is lost by forming HNO_3 which is then scavenged when precipitation occurs.

Atmospheric methane is depleted by oxidation through increased OH concentrations, initially through the same reaction that forms ozone, and additionally once NO_x levels are reduced but ozone levels are still high from a reaction between $O(^1D)$ and water vapour. In total 14 reactions and groups of reactions are tracked: one for ozone production, one for ozone destruction, one for HNO_3 production, three for OH production, five for OH destruction (including methane oxidation), one for HO_2 production, and two for HO_2 destruction (more details are given in Grewe et al., 2014b; Grewe et al., 2017c).

The AIRTRAC submodel tracks the mass development of water vapour, NO_x, O_3, HNO_3, OH, HO_2, and depleted methane in each air parcel. The model integration time is 90 days, which covers most of the short-term responses. An extrapolation of the remaining terms is used to cover the whole response. For ozone the RF is directly calculated during the model simulation using the radiation submodel (Dietmüller et al., 2016) for other species mass related state-of-the art relations are used (Grewe et al., 2014b). Note that the adjusted RF was used in deriving the CCFs for all species except for contrails, which are not regarded in this work.

To select the adequate climate impact metric, the question to be answered must be specified (Grewe and Dahlmann, 2015). Grewe et al. (2014b) selected a number of preferred metrics to answer three distinct questions. Here, we are focussing on the question: “What is the short-term climate impact of consistently applying the REACT4C re-routing strategy?”. The metric used to answer this question is F-ATR20, the average temperature response over 20 years given future increasing emissions (FA1 scenario, Penner et al., 1999). The change in the routing strategy is reflected by applying a change in the emissions in the FA1 scenario and evaluating the change in climate impact. Grewe et al. (2014a) tested two other metrics (pulse emission combined with global warming potential and a time horizon of 20 as well as 100 years), which lead to comparable results. This metric in [K] normalised by the size of the unit emission in [kg] is thus the CCF in $[\mathrm{K\,kg^{-1}}]$, i.e. the 4-D variation of the global-average climate impact from a unit local emission.

Grewe et al. (2014b) compared the temporal development of NO_x, methane and ozone in the air parcels with results from Stevenson et al. (2004) and showed that the results compared well. Further details on the approach for simulating CCFs are given in Grewe et al. (2014b).

2.4. Algorithm development and selection

As the CCFs are calculated on a $6 \times 7 \times 4$ irregular grid with fixed pressure coordinates and as the weather in the EMAC background model is made available in the T42L41 resolution, the weather data is trilinearly interpolated to the CCF grid.

The following method is applied three times for water vapour, ozone, and methane climate impacts, respectively (ozone and methane impacts from NO_x emissions are analysed separately due to the differing chemical mechanisms and timescales):

1. Literature is reviewed to pre-select variables to be included in the analysis. Further selection is done on the basis of histograms and kernel density estimations (KDEs) of the interpolated weather data, such as temperature and precipitation, to eliminate sparse or clearly redundant variables.
2. A scatter plot matrix of the CCF data and all selected variables is generated to compare univariate scatter plots of each combination, histograms and KDEs of each variable, and Spearman rank coefficients for each combination.
3. Zero-dimensional, instantaneous regression is performed where multiple predictors and non-linear regressions are considered. Four candidate algorithms are developed from promising (combinations of) predictors based on scatter plot matrix analysis.
4. A final algorithm is selected via a trade-off, which is based on the requirements of algorithm-based CCFs as we currently foresee.

Note that a full description can be found in Manen (2017). In Sections 3 and 4, we briefly describe candidate variables and concentrate on steps 3 and 4 for clarity. The trade-offs in step 4 are based on the qualitative evaluation of five criteria: the pattern of the residua, accuracy, external veracity, background, and parsimony (for more details, see below).

The most important requirement for aCCFs is that deviations from the simulated CCFs do not lead to incorrect aircraft routing decisions when applied. To this end, the pattern of the residua is considered by examining the mean value across altitudes and weather patterns of the range of the residua within each latitude-longitude field. The lower this number is, the less variation in

residua per 2-D field. To compare the absolute accuracy across all data of the algorithms, the Residual Standard Error (RSE) and adjusted regression coefficient R^2 (adjusted R^2 is used to reduce the effect of the numbers of predictors on R^2) are calculated. As the REACT4C CCFs cover a limited geographical and temporal domain, literature and knowledge of atmospheric circulation are used to estimate the applicability and veracity of the algorithms in other situations. A similar approach is used to estimate the strength of the causal relationship between the dependent and independent variables. The last categories considered are parsimony, i.e. minimising the amount of parameters, external veracity, the potential applicability to an area outside of the REACT4C domain, and mechanistic background, the ability to link the correlation to physical processes.

To summarise, our very detailed data set not only describes the meteorology and chemical composition of the atmosphere, but also has information on the expected climate impact from a local emission of water vapour and NO_x (CCFs, Section 2.3). We make use of this to derive formulas, which describe the relation between the meteorology at the time of emission and its climate impact (Section 2.3).

3. Approximations of the climate impact from water vapour emissions

In terms of dimensions, the CCF data for water vapour emissions vary far more with pressure than latitude, longitude or weather pattern. Lower pressure (thus higher altitude) emissions lead to higher mean CCF values with a non-linear trend and a corresponding trend in the range of results (i.e. heteroscedasticity). Results for summer weather patterns are on average lower than for winter weather patterns, and most notably the non-linear trend with pressure and heteroscedasticity are weaker in summer. This is presumed to be related to the increased altitude (thus lower pressure) of the tropopause in summer. Higher CCF values for emissions into the stratosphere can be explained physically by weaker removal processes in the stratosphere (e.g. Lee et al., 2010), thus longer lifetime of the emitted water vapour and a higher RF. Box plots of the water vapour CCFs are given in the Supplement.

Strong variability with altitude is consistent with results from Frömming et al. (2012), where the vertical trend in water vapour climate impact was of similar magnitude as for other species while the absolute magnitude is smaller. The non-linear trend does not agree with results from Wilcox et al. (2012) who found an almost linear trend. This is not readily comparable, however, as they present one data point for the entire Northern Hemisphere per altitude in a subset of the pressure range used here.

3.1. Candidates

Grewe et al. (2014b) use a linear relationship to relate the remaining emitted water vapour mass to adjusted RF, hence all variability in the CCF data must be due to varying removal rates in the background model at locations the different air parcels are transported to. Thus the underlying hydrological physics in the ECHAM5 base model (see Roeckner et al., 2003), are very likely to be correlated to the CCF data. All variables related to precipitation, humidity and cloud physics from all relevant EMAC sub-models are included in the scope. After elimination through histogram analysis, 30 variables are left. Three types of variables are pursued:

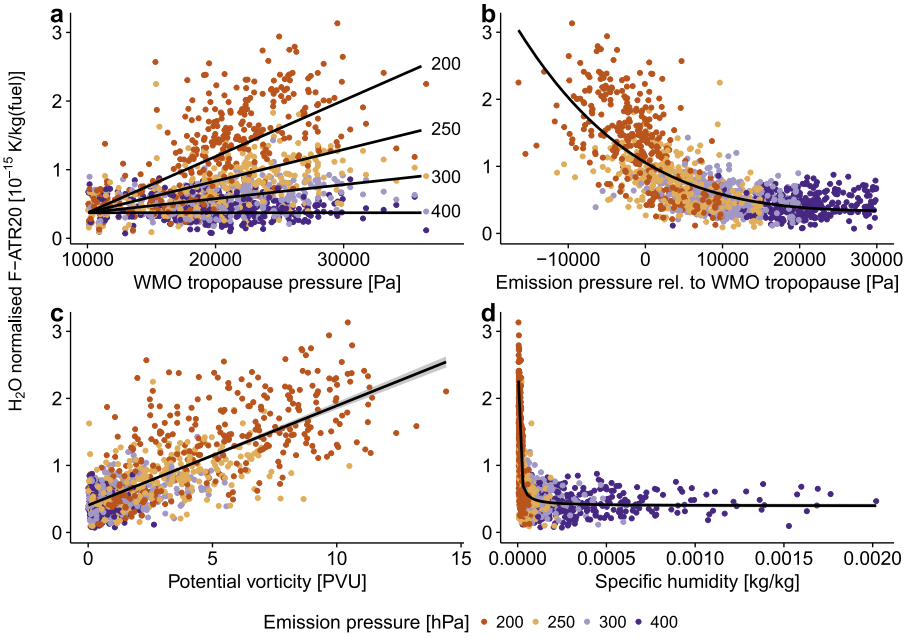

Fig. 2. Relationships between simulated water vapour CCF data and relevant weather variables with four algorithm candidates shown as black curves: (a) bilinear dependence on WMO tropopause pressure and emission pressure, plotted once per emission pressure for clarity, (b) quartic dependence on emission pressure relative to WMO tropopause, (c) linear dependence on PV, (d) inverse dependence on specific humidity.

general meteorology (e.g. wind velocity), tropopause (e.g. dynamic tropopause pressure), and precipitation (e.g. vertically integrated cloud ice). In the end, four most promising relationships between the CCF data and weather data emerged (Section 3.2, Fig. 2).

3.2. Algorithms

For each of the four relationships in Fig. 2 an algorithm was devised using regression analysis, the results of which are shown as black curves in the figure. The respective forms of the curves in figures (a)–(d) are:

$$\text{F-ATR20}_{\text{H}_2\text{O}} = \beta_0 + \beta_1 \times (p_{tp,\text{WMO}} - 10,000) \times (40,000 - p_{em})^2 + \epsilon \tag{1}$$

$$\text{F-ATR20}_{\text{H}_2\text{O}} = A + B \times (p_{em} - p_{tp,\text{WMO}} - C)^4 + \epsilon \tag{2}$$

$$\text{F-ATR20}_{\text{H}_2\text{O}} = \beta_0 + \beta_1 \times PV + \epsilon \tag{3}$$

$$\text{F-ATR20}_{\text{H}_2\text{O}} = \beta_0 + \beta_1 \times q^{-1} + \epsilon \tag{4}$$

Here $p_{tp,\text{WMO}}$ is the pressure of the World Meteorological Organisation (WMO) defined thermal tropopause and p_{em} is the emission pressure, both in [Pa]. The abbreviation PV is potential vorticity in [PVU] and q is specific humidity in [kg kg^{-1}]. Parameters β_x are for linear regression, A–C are for non-linear regression and ϵ is the unexplained variation of the original CCF data. The variables F– ATR20, p, PV, and q are functions of (x, y, z, t), but this is omitted in the description for legibility. Values and uncertainties of the parameters are listed in Appendix A.

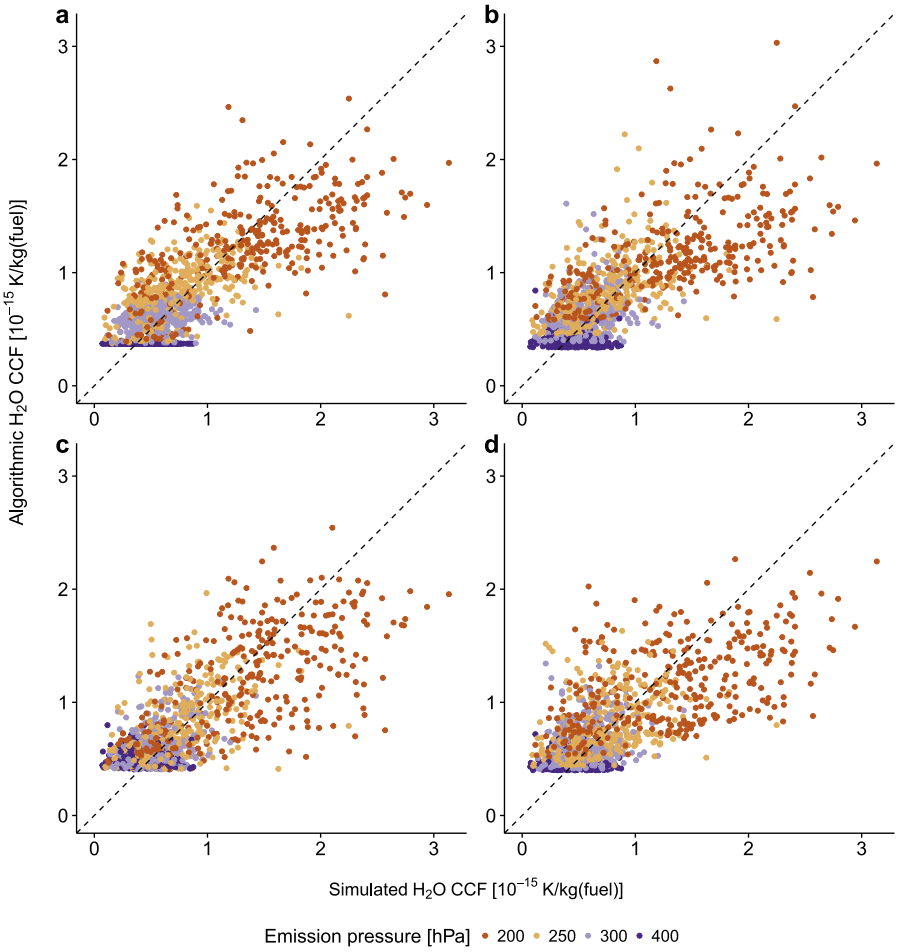

Fig. 3. Comparisons of algorithmic CCF results for water vapour with the simulated data, (a) bilinear dependence on WMO tropopause pressure and emission pressure, (b) quadratic dependence on emission pressure relative to WMO tropopause, (c) linear dependence on PV, (d) inverse dependence on specific humidity.

Table 2
Overview of results of the subjective water vapour algorithm trade-off, per algorithm and category. If three or more results are distinct, they are ranked into + , ± and −. If only two distinct categories are identified, only + and − are used.

Algorithm	Pattern	Accuracy	External veracity	Background	Parsimony
$(p_{em} - p_{tp,\mathrm{WMO}})^4$	−	−	±	±	−
$p_{tp,\mathrm{WMO}} \times p_{em}^2$	+	+	−	−	−
PV	+	+	+	±	+
q^{-1}	−	±	±	+	±

3.3. Assessment

Fig. 3 shows each of these algorithms' results compared to the original CCF data. Overall the pattern is similar. Data for 400 hPa emissions appear to be predicted correctly but the use of coefficients β_0 or A produces a clear minimum at the low end of CCF values. Data for 300 and 250 hPa emissions appear to be correctly predicted. Data for 200 hPa emissions show a lower correlation compared to the lower emission altitudes.

The tropopause algorithms (Figs. 3a and b) appear to show a polynomial remaining trend. The PV algorithms (c) appear to have the weakest remaining trend, and the humidity algorithm (d) appears to show a linear remaining trend.

Table 2 presents an overview of the four algorithms' strengths and weaknesses. The 5 categories are evaluated either based on data (e.g. RSE) or on visual inspection (heteroscedasticity) The spread of the residua (pattern) is 10% smaller for the algorithm based on PV and the combination of tropopause pressure and emission pressure. The residual standard error (accuracy) is also smallest for these two algorithms with $3.2–3.3 \times 10^{-16}$ K/kg(fuel). The external veracity is naturally difficult to examine, though some indications may be given. For example a very low humidity might largely overestimate the climate impact in the algorithm based on specific humidity and the algorithm based on the difference of the emission pressure to the tropopause pressure might risk exceeding the minimum value for high tropopause and a low altitude emission situation, whereas the algorithm based on PV seems to provide no obvious outliers. PV is also a well-known meteorological parameter with high values in the stratosphere and low values in the troposphere, resembling findings that the climate impact should decrease towards the tropics and increase with altitude (Grewe and Stenke, 2008; Wilcox et al., 2012). The PV algorithm is the only one that scores well consistently and is chosen here as the final algorithm with an adjusted regression coefficient R^2 of 0.59.

The final form of the water vapour algorithmic CCF (aCCF) in $[\mathrm{K\,kg(fuel)^{-1}}]$ is:

$$\begin{aligned} &\text{for a point } (x, y, z) \text{ with } PV = PV(x, y, z, t):\\ &\mathrm{aCCF}_{\mathrm{H_2O}}(PV) = 4.05 \times 10^{-16} + 1.48 \times 10^{-16} \times |PV|\\ &\mathrm{aCCF}_{\mathrm{H_2O}}(PV) \approx \text{F-ATR20}_{\mathrm{H_2O}}(x, y, z, t) \end{aligned} \tag{5}$$

In the Southern Hemisphere, PV is by definition negative while it is expected that some of the trends in water vapour CCFs are similar. For this reason the absolute value of the PV is used.

4. Approximations of the climate impact from NO_x emissions

4.1. Candidates

The impact of a NO_x emission on ozone depends on a number of factors, such as local NO_x chemistry (Stevenson et al., 2004), i.e. sunlight, temperature and background concentrations of chemical species, especially NO_x. Convection and lightning also plays a role, since it effectively vertically mixes trace gases and impacts the background NO_x concentration by emissions of NO_x from lightning (Berntsen and Isaksen, 1999; Grewe et al., 2002). The hydrological cycle is also important, since the wash-out of nitrogen species limits the ozone production (e.g., Gauss et al., 2006). Hence the general meteorology and circulation, solar radiation, background chemistry and lightning indicators where chosen as predictors for the NO_x climate impact. After analysing scatter plots (not shown, see also Section 2.4), temperature, geopotential, specific humidity, and solar radiation remained as most promising candidates. This shows that other variables, such as lightning and background concentrations at the time of emission are not important for the temporal evolution of the ozone and methane response. Instead, we found that variables that might indicate the future transport pathway are much more important.

The impact of a NO_x emission on methane is largely linked to the ozone formation process, since in this case the production of ozone leads to an enhancement of the OH concentration and thereby a depletion of methane, since the reaction of methane with OH is the main tropospheric loss reaction (e.g., Lee et al., 2010). However, in a second phase the enhancement of ozone caused by the NO_x emission will also enhance the OH concentration, since ozone is a precursor for OH, even if the emitted NO_x is already removed from the atmosphere (e.g. Grewe et al., 2017c). Hence, the most promising candidates for a methane algorithm were found to be similar to those for ozone: geopotential, solar radiation, potential temperature, and the ozone climate change function itself. The latter is included because a correlation between the ozone and methane response is found in many studies (Lee et al., 2010; Holmes et al., 2013). Since the variability of the methane response is much smaller than for ozone also a constant response is tested in addition (see below).

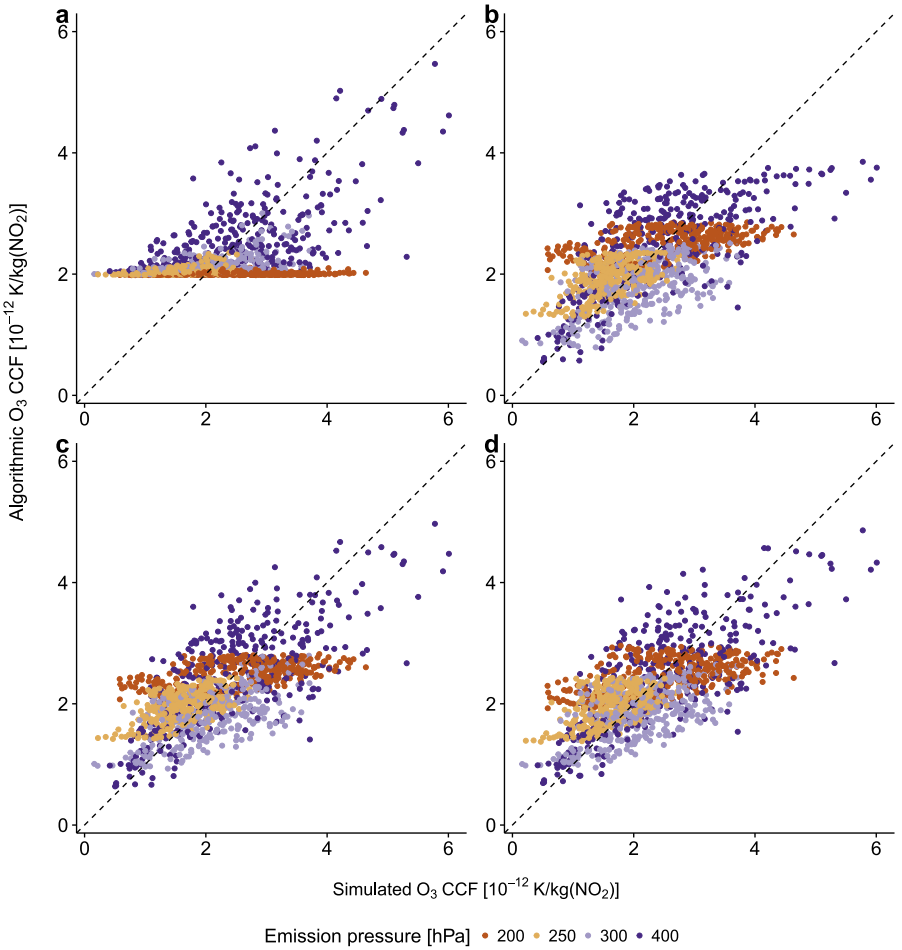

Fig. 4. Comparisons of algorithmic CCF results for ozone with the simulated data, (a) linear dependence on specific humidity, (b) bilinear dependence on temperature and geopotential, (c) trilinear dependence on temperature, geopotential and specific humidity, (d) quadrilinear dependence on temperature, geopotential, specific humidity and irradiance.

4.2. Ozone algorithms

The four emerging candidate algorithms based on the pre-analysis are:

$$\text{F-ATR20}_{O_3} = \beta_0 + \beta_1 \times q + \epsilon \tag{6}$$

$$\text{F-ATR20}_{O_3} = \beta_0 + \beta_1 \times T + \beta_2 \times \Phi + \beta_3 \times T \times \Phi + \epsilon \tag{7}$$

$$\text{F-ATR20}_{O_3} = \beta_0 + \beta_1 \times T + \beta_2 \times \Phi + \beta_3 \times q + \beta_4 \times T \times \Phi + \epsilon \tag{8}$$

$$\text{F-ATR20}_{O_3} = \beta_0 + \beta_1 \times T + \beta_2 \times \Phi + \beta_3 \times q + \beta_4 \times F_{in} + \beta_5 \times T \times \Phi + \epsilon \tag{9}$$

Here T is the atmospheric temperature in [K], Φ is the geopotential in [$m^2\,s^{-2}$], and F_{in} is the solar irradiance or incoming solar flux at the top of the atmosphere (no vertical variation, maximum over latitude band, i.e., local noon values) in [W^{-2}]. Values and uncertainties of the parameters are listed in Appendix A. An explanation on how to estimate the solar irradiance is given in Appendix B.

4.3. Ozone assessment

Fig. 4 shows correlations between the simulated data from REACT4C and the algorithmic CCFs. Except for the algorithm based on specific humidity (a), all correlations are similar (b–d). The spread of the residua ranges between $2.3 \cdot 10^{-12}$ K/kg(NO_2) and $2.5 \cdot 10^{-12}$ K/kg(NO_2), with best values for the algorithms combining temperature, geopotential, and humidity (see also Table 3 for a qualitative assessment). The adjusted regression coefficient R^2 is smaller (0.2) for the specific humidity based algorithm and has values between 0.42 and 0.45 for the others. The temperature and geopotential based algorithms might be expanded to other regions,

Table 3
Overview of results of the subjective ozone algorithm trade-off, per algorithm and category. If three or more results are distinct, they are ranked into + , ± and −. If only two distinct categories are identified, only + and − are used.

Algorithm	Pattern	Accuracy	External veracity	Background	Parsimony
q	−	−	−	−	+
$T \times \Phi$	±	±	+	+	±
$T \times \Phi + q$	+	+	±	−	−
$T \times \Phi + q + F_{in}$	+	+	±	−	−

whereas large values of specific humidity might cause unrealistic large values in the q-based algorithmic CCF.

Hence the final ozone algorithmic CCF in [K kg$(NO_2)^{-1}$] is based on temperature and geopotential, only:

For an atmospheric location (x, y, z) at time t with $T = T(x, y, z, t)$ and $\Phi = \Phi(x, y, z, t)$:

$$\begin{aligned}
\widetilde{\mathrm{aCCF}}_{O_3}(T, \Phi) = & -5.20 \times 10^{-11} + 2.30 \times 10^{-13} \times T + 4.85 \times 10^{-16} \times \Phi \\
& - 2.04 \times 10^{-18} \times T \times \Phi \\
\mathrm{aCCF}_{O_3}(T, \Phi) = & \begin{cases} \widetilde{\mathrm{aCCF}}_{O_3}(T, \Phi) & \text{for } \widetilde{\mathrm{aCCF}}_{O_3}(T, \Phi) > 0 \\ 0 & \text{else} \end{cases} \\
\mathrm{aCCF}_{O_3}(T, \Phi) \approx & \ \text{F-ATR20}_{O_3}(x, y, z, t)
\end{aligned} \tag{10}$$

The extra step is included to ensure positive CCF results. The adjusted regression coefficient R^2 of this algorithm within the REACT4C dataset is 0.42.

4.4. Methane algorithms

The four algorithms for the methane CCFs, based on the candidate analysis (see Section 4.1) are:

$$\text{F-ATR20}_{CH_4} = \beta_0 + \epsilon \tag{11}$$

$$\text{F-ATR20}_{CH_4} = \beta_0 + \beta_1 \times \Phi + \epsilon \tag{12}$$

$$\text{F-ATR20}_{CH_4} = \beta_0 + \beta_1 \times \Phi + \beta_2 \times F_{in} + \beta_3 \times \Phi \times F_{in} + \epsilon \tag{13}$$

$$\text{F-ATR20}_{CH_4} = \beta_0 + \beta_1 \times \text{F}-\text{ATR20}_{O_3} + \beta_2 \times T_{pot} + \epsilon \tag{14}$$

Here F-ATR20_{O_3} is the simulated (not algorithmic) REACT4C ozone CCF data in [K kg$(NO_2)^{-1}$], and T_{pot} is the potential temperature in [K]. Values and uncertainties of the parameters are listed in Appendix A.

4.5. Methane assessment

Fig. 5 shows the correlations of the four algorithms with the REACT4C data. Clearly 3 different patterns can be seen: the constant algorithm obviously produces a poor correlation pattern, the two algorithms which include the geopotential show only a very limited variation for individual emission pressures, whereas the algorithm based on the ozone response shows the best correlation pattern (see also Table 4). The accuracy (RSE) is 0, 0.13, 0.17, and 0.29 for the four algorithms, respectively. The algorithm based on a constant is likely not to be a good choice, since there are clear spatial variations (Grewe and Stenke, 2008; Köhler et al., 2013). The algorithm related to the ozone response is highly dependent on the ozone methane relation in the investigated region (North Atlantic Flight Corridor). And the ratio between the ozone and methane feedback also shows large regional variability (Grewe and Stenke, 2008).

In this case the choice of the algorithm is not so clear compared to the previous cases. Although clearly the algorithm which is based on the ozone response scores best, these data are not readily available in weather forecasts and the same algorithm based on the algorithmic CCFs for ozone instead of the simulated REACT4C CCFs scores considerably worse. Pattern and accuracy are slightly better for the algorithm which is based on the geopotential and solar radiation, compared to the remaining ones.

The final form of the methane algorithmic CCF in [K kg$(NO_2)^{-1}$] hence is: For an atmospheric location (x, y, z) at time t with $F_{in} = F_{in}(x, y, z, t)$ and $\Phi = \Phi(x, y, z, t)$:

$$\begin{aligned}
\widetilde{\mathrm{aCCF}}_{CH_4}(\Phi, F_{in}) = & -9.83 \times 10^{-13} + 1.99 \times 10^{-18} \times \Phi - 6.32 \times 10^{-16} \times F_{in} \\
& + 6.12 \times 10^{-21} \times \Phi \times F_{in} \\
\mathrm{aCCF}_{CH_4}(\Phi, F_{in}) = & \begin{cases} \widetilde{\mathrm{aCCF}}_{CH_4}(\Phi, F_{in}) & \text{for } \widetilde{\mathrm{aCCF}}_{CH_4}(\Phi, F_{in}) < 0 \\ 0 & \text{else} \end{cases} \\
\mathrm{aCCF}_{CH_4}(\Phi, F_{in}) \approx & \ \text{F-ATR20}_{CH_4}(x, y, z, t)
\end{aligned} \tag{15}$$

The extra step is included to ensure negative CCF results. The adjusted regression coefficient R^2 of this algorithm within the REACT4C dataset is 0.17.

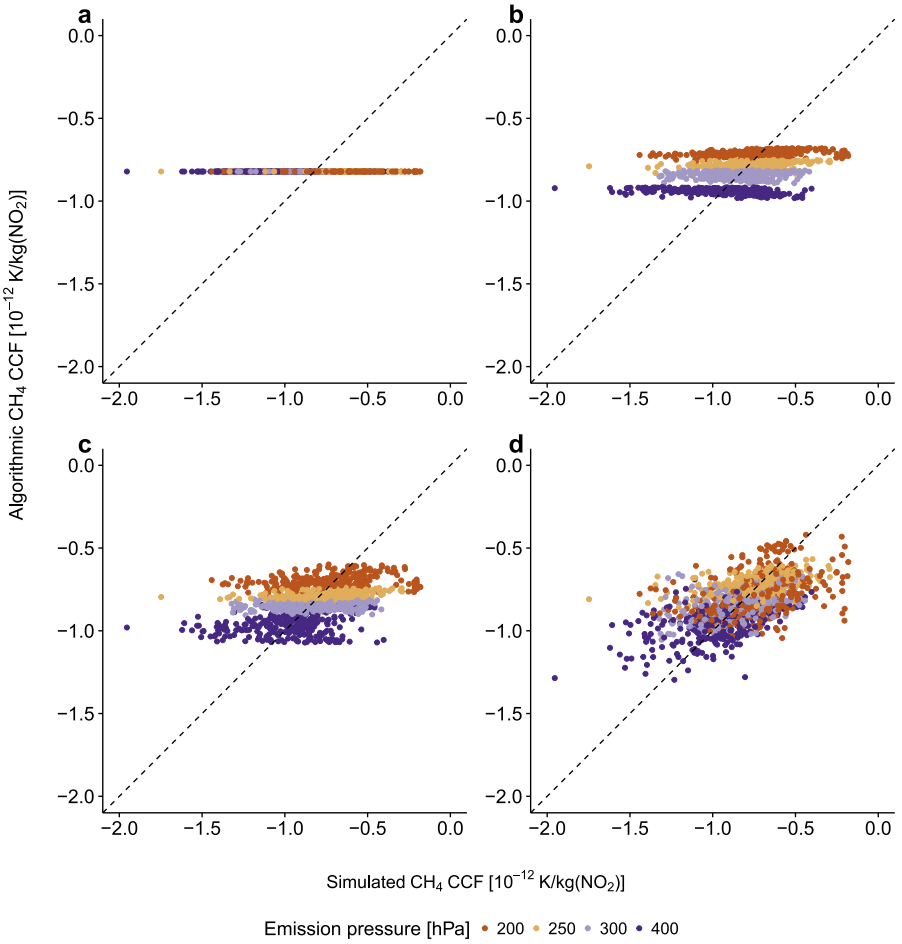

Fig. 5. Comparisons of algorithmic CCF results for methane with the simulated data, (a) constant, (b) linear dependence on geopotential, (c) bilinear dependence on geopotential and irradiance, (d) bilinear dependence on potential temperature and ozone CCF. One outlier was removed from the plot for legibility: the REACT4C simulation gives almost -3.2×10^{-12} K/kg(NO_2) for this location and none of the algorithms accurately represent this.

Table 4
Overview of results of the subjective methane algorithm trade-off, per algorithm and category. If three or more results are distinct, they are ranked into + , ± and −. If only two distinct categories are identified, only + and − are used. *Strongly depends on application.

Algorithm	Pattern	Accuracy	External veracity	Background	Parsimony
Constant	−	−	−	−	+
Φ	−	±	+	±	+
$\Phi \times F_{in}$	±	±	±	±	−
F-ATR20$_{O3}$ + T_{pot}	+	+/±*	−	+	±

Fig. 6 shows the comparison of the simulated correlation of ozone and methane CCFs (left) with the respective values of the aCCFs (right). Clearly, the correlation shows a smaller variability for the aCCFs data compared to the CCFs. The tendencies that (1) the ozone CCFs show a larger variability than the methane CCFs and (2) that the difference between summer (green) and winter (red) are well captured by the algorithmic approach. Hence the total NO_x effect, i.e. the sum of the ozone and methane aCCFs, is captured well by the algorithmic CCFs.

Note that effects such as the feedback from the methane change to the ozone productivity, the so-called primary mode ozone (PMO) (Wild et al., 2001; Derwent et al., 2001; Myhre et al., 2013) and the change in stratospheric water vapour due to the change in tropospheric methane (Myhre et al., 2007) are not included here, but might simply be regarded as a offset of the methane algorithmic climate change function, i.e. a linear scaling of the methane aCCF, since those are primarily driven by the methane change. This procedure is frequently applied (e.g. see Skowron et al., 2013).

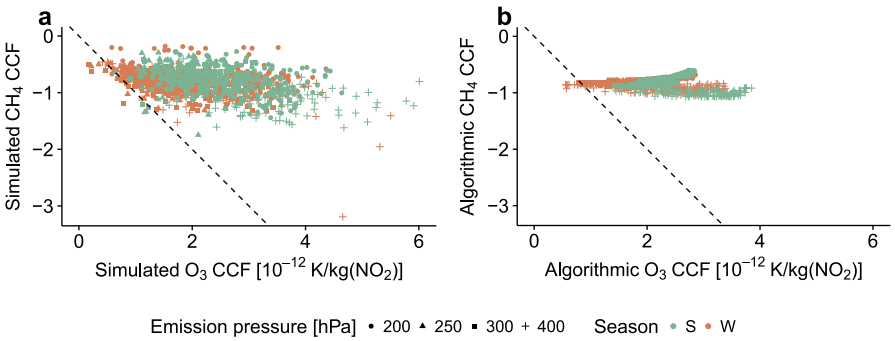

Fig. 6. Relationship between ozone and methane climate impact from the same uniform NO_x emission, (a) REACT4C simulation results, (b) algorithmic results. The dotted line represents net-zero CCF from a NO_x emission, i.e. $aCCF_{CH_4} + aCCF_{O_3} = 0$.

5. Comparison of algorithmic and high fidelity climate change functions

In the previous sections we developed functional relationships between data readily available from numerical weather forecast models, i.e. algorithmic climate change functions, and climate change functions calculated for 8 specific days, representing 8 distinct weather patterns. Correlations between data based on either approach are presented in Figs. 3–5. Here, we first discuss the general differences between the CCFs and aCCFs in Section 5.1 and then present comparisons of the spatial distributions in Section 5.2, which are important since these gradients largely drive the selection of aircraft trajectories when optimising them for low climate impacts. We focus on one of the analysed days, the weather pattern WP1, only. Other weather patterns have similar features (not shown).

5.1. General characteristics

Table 5 gives an overview on the characteristics of aCCFs and CCFs. The CCFs can be used for the 8 specific weather situations they are designed for whereas the aCCFs have the flexibility to be applied for any arbitrary day, largely increasing the applicability and flexibility. The CCFs are designed for the North-Atlantic and only there data are available. Since the meteorology is in general similar along one latitude, the aCCFs are applicable in the northern hemisphere extra-tropics. Since aCCFs rely on meteorological input parameters only, they can easily be implemented in numerical weather prediction models (NWPs). Any extension of the CCF dataset with respect to date and region and any extension of the aCCFs with respect to the region require large computational efforts. However, as soon as algorithms are established, they have a much larger flexibility in the application compared to CCFs.

5.2. Comparison of patterns

Fig. 7 shows the horizontal patterns of the CCFs (left) and aCCFs (right) for water vapour (top), ozone (mid), and methane (bottom). The water vapour CCF and aCCF both show low values at lower latitudes and a ridge of larger values reaching from higher to lower latitudes from West to East. However, the ridge based on the aCCF values is more tilted. In addition, the CCF data seem to be noisier, e.g. there is an isolated maximum at 40°N and 45°W. It remains to be shown whether such local patterns are based on uncertainties in the modelling approach or on actual physical processes. Similarly, the vertical profiles of the water vapour CCFs and aCCFs agree in their general pattern (Fig. 8), with a clear gradient from lower altitude to higher altitudes and lower latitudes to higher latitudes. This dependency of the climate impact on the altitude of the emission agrees well with previous studies (Grewe and

Table 5
Comparison of the characteristics of CCFs and aCCFs.

	CCF	aCCF
Characteristics		
Meteorology	8 specific simulated days	Arbitrary days
Horizontal coverage	North Atlantic	30°N-90°N
Implementation	Unflexible fixed dataset	Easily implemented in NWPs
Extention	Large computational effort with a limited applicability to the chosen date or area	Large computational effort and large effort to derive new algorithms for other areas, however when established, they have a large flexibility in the application
Verification	Comparison of general patterns with literature	Dedicated numerical simulation with a climate-chemistry model including a traffic simulator and dedicated diagnostics
Quality		
CO_2	+ +	+ +
H_2O	+ +	+ +
NO_x-O_3	+	o
NO_x-CH_4	+	−

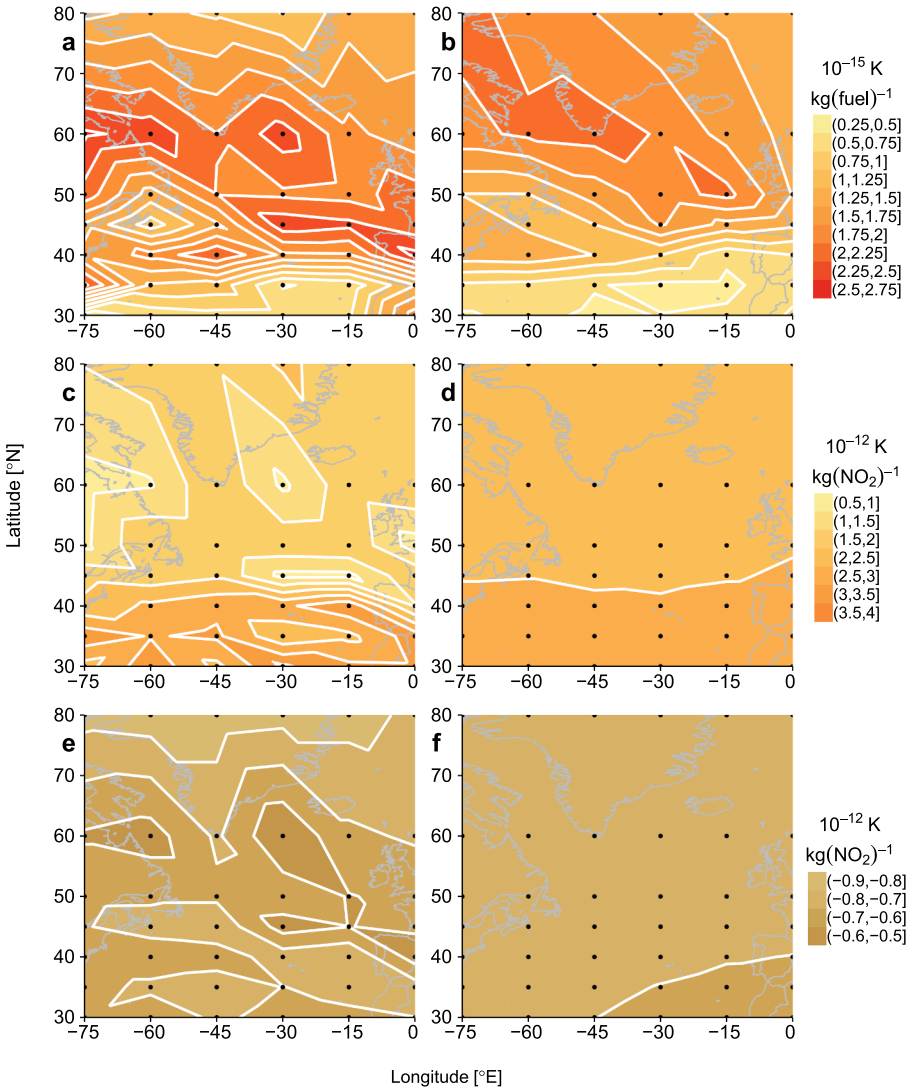

Fig. 7. Interpolated heatmaps of the CCFs for WP1, emission at 200 hPa, (a) REACT4C simulated water vapour, (b) algorithmic water vapour, (c) REACT4C simulated ozone, (d) algorithmic ozone, (e) REACT4C simulated methane, (f) algorithmic methane. The black dots represent emission locations in the REACT4C set-up.

Stenke, 2008; Frömming et al., 2012; Wilcox et al., 2012), which analysed this effect on a more climatological, rather than weather-related basis. Grewe and Stenke (2008) showed a latitudinal dependency of the water vapour emission effect, which basically follows the location of the tropopause and the results for the water vapour aCCF (Fig. 8) generally agree in this respect.

In Sections 3 and 4, we showed that aCCFs represent the spatial variability of the CCFs much better in the case of water vapour than for ozone and even worse for methane. This can also be seen in Figs. 7 and 8. Although the general horizontal gradient is well represented by the ozone aCCFs, with large (small) values in lower (higher) latitudes, smaller-scale patterns, such as the minimum around 60°N and 60°W, are not reproduced. The vertical profiles of the ozone aCCFs show again similarities with ozone CCFs, such as increasing values from 300 hPa to 200 hPa and from high to low latitudes. The variability in the methane CCFs is an order of magnitude smaller and hence less important to be captured by the aCCFs. Therefore, the low representation of the spatial pattern (Fig. 7) is expected to have a low impact on climate-optimised routings, when using aCCFs. The climatological response of a NO_x emission on ozone was found to be larger when the emission location is at lower latitudes compared to high latitudes (Köhler et al., 2013; Grewe and Stenke, 2008), which generally agrees with our findings for this specific weather situation. Köhler et al. (2008) and Grewe and Stenke (2008) showed that the ozone induced climate impact of a NO_x emission increases with altitude, showing a sharp gradient at the tropopause. Here we find similar characteristics (Fig. 8), an increase in the climate impact between 300 hPa and 200 hPa and an increase towards lower latitudes. However, a distinct difference occurs: at lower emission altitudes (high pressure levels of 400 hPa), the climate impact increases again. It might be that this feature is solely caused by the distinct weather situations, selected here. However, since it appears in most of the 8 weather situations (not shown), other reasons might be more likely. We have

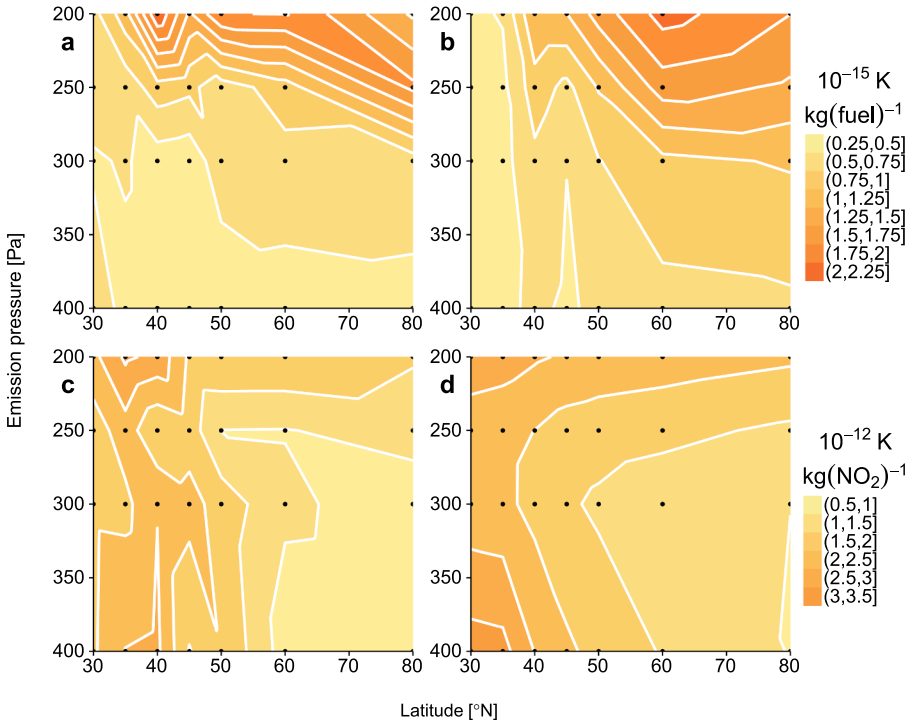

Fig. 8. Comparison of vertical profiles of the CCFs (left) and aCCFs (right) for WP1, with emission at 315°E. (a) REACT4C simulated water vapour, (b) algorithmic water vapour, (c) REACT4C simulated ozone, (d) algorithmic ozone. The black dots represent emission locations in the REACT4C set-up.

identified that this specific vertical structure is also affected by the conversion of the radiation change into the adjusted radiative forcing (Grewe et al., 2014b).

To summarise, the good correlation of the meteorology at the time and location of emission with the impact of the emissions on water vapour and ozone strongly indicates that meteorology largely controls the transport pathway and by this the impact on climate. Emitted water vapour remains longer in the troposphere the closer to or deeper into the stratosphere it is emitted. NO_x is more easily transported to the tropics with a larger increase in ozone due to the more active chemistry, if emitted within a high pressure system, when compared to the area west of it (Frömming et al., 2019; Grewe et al., 2017a). Similar to water vapour, NO_x effects are stronger for emissions at higher altitude. The dependence of the ozone aCCFs on the geopotential and temperature appears to reflect this relation.

6. Discussion: uncertainties and validation approaches

Clearly, the CCFs are associated with various sorts of uncertainties. The aCCFs naturally inherit these uncertainties and uncertainties in the derivation of the aCCFs have a compounding effect. The latter were quantified in the previous section and details are given in the appendix. Here we focus on uncertainties in the CCFs and the use of aCCFs, before qualitatively assessing the individual aCCFs and before addressing ways to verify the aCCFs.

In the calculation of the CCFs, a number of processes are taken into account, starting with atmospheric transport, chemistry, microphysics and radiation. A thorough validation of EMAC was undertaken in Jöckel et al. (2010, 2016) and a comparison, specific to this application, of individual quantities with either other modelling studies or observations was performed in Grewe et al. (2014b) to generally show that the results are reasonably agreeing with previous work. This includes, e.g., the evolution of ozone and methane concentrations, contrail properties, contrail radiation impacts, and overall metric results.

However, a validation of climate change functions, in the original version as well as the algorithmic derivatives, i.e. a direct intercomparison of the expected climate impact, is principally not feasible (Grewe et al., 2014b) and to show that the use of aCCFs for climate-optimised aircraft trajectories is meaningful and will provide the expected result, several steps were and will have to be undertaken in addition to the above mentioned validation of the basic model and the extensions used to calculate the CCFs (Grewe et al., 2014b).

We have identified two possibilities to verify aCCFs: (1) the calculation of climatological aCCFs, which can be compared to literature and (2) a closure experiment, testing that the climate impact of aviation is reduced when using the aCCFs in the optimisation of the aircraft trajectories. For calculating climatological aCCFs a long-term simulation is needed, for every timestep aCCFs are calculated, and an annual mean is derived from such a simulation. This reflects the annual mean sensitivity of e.g. an ozone

response and its RF from an emission at a certain altitude and latitude. These values can be compared to findings presented in literature (e.g. Grewe and Stenke, 2008; Köhler et al., 2008). First results show a reasonable agreement of the gradients of these sensitivities (Yin et al., 2018) and a more detailed analysis is in preparation.

For the closure experiment a chemistry-climate model which allows for an air traffic optimisation using aCCFs is required, which also allows for detecting small changes in the, e.g., ozone concentration. Yin et al. (2018) made use of the chemistry-climate model EMAC (Jöckel et al., 2016) with its submodel AirTraf (Yamashita et al., 2016) for the air traffic simulation within EMAC and a tagging scheme for detecting small chemical changes (Grewe et al., 2017c). First simulations show that a reduction of the ozone radiative forcing from aviation can be achieved, when using the aCCFs (here only NO_x-ozone aCCFs) in the optimisation of the air traffic flow in AirTraf.

These two approaches show a testing to confirm that the developed aCCFs reasonably reflect the pattern of the sensitivity of an emission for the near surface temperature change. We think, based on our data analysis (high value of R^2) and based on the physical interpretation of the data (potential vorticity as a predictor reflects the turn-around times of water vapour), that the water vapour aCCFs reflect the sensitivity of a water vapour emission on expected water vapour concentration changes and its impact on the radiation budget (Table 5). The NO_x-ozone aCCFs have a lower adjusted R^2. Grewe et al. (2017a) indicated that the meteorology at the time of emission very much determines the transport pathway of the emitted species and the meteorology is well described by the geopotential and temperature, the predictors for this aCCF. Hence we rate the reliability slightly lower than that of water vapour. Since the NO_x-methane adjusted R^2 is poor and the physical and chemical interpretation of the predictors is more vague, this aCCF is rated qualitatively worse than the others (Table 5).

Hence, there are significant uncertainties, though also ways to address their impact via dedicated simulations (see above) rather than giving clear uncertainty ranges. However, when applying these aCCFs a couple of other aspects have to be taken into account, such as the accuracy of the weather forecast and the climate objective. The latter is important, since if a different climate objective is raised other climate metrics might be relevant and this will very likely lead to other results (e.g. Fuglestvedt et al., 2010; Grewe and Dahlmann, 2015). Note that for the climate objective we raised ("What is the short-term climate impact of consistently applying the REACT4C routing-strategy?") there are some climate metrics which are applicable, but which lead to similar results (Grewe et al., 2014a). Other climate metrics may lead to other results, but also answer other questions.

7. Conclusion and outlook

One possibility to reduce the climate impact of aviation is the avoidance of climate sensitive regions in which the non-CO_2 effects, such as contrails and ozone production, are exceptionally strong. The planning of climate-optimised routes requires information on the climate impact of a local emission. This information is provided by climate change functions, which require large computing resources and limit thereby the use in daily flight planning. Here we present algorithmic climate change functions for water vapour and NO_x emissions, which are based on data available from numerical weather prediction and hence allowing forecasts in the same frequency as weather forecasts. Another way to reduce computing time is to use climatological CCFs instead of weather-dependent CCFs (e.g. Grewe et al., 2017a). However, the climate impact reduction potential is smaller when using the climatological CCFs, than taking advantage of the actual weather situation (Grewe and Linke, 2017). Note that various means of implementation are discussed in literature, which are all based on CCFs, or aCCFs, either on a climatological or weather-dependent basis. Besides market-based measures (Grewe et al., 2017b), the seasonal closure of entire parts of the airspace (climate restricted airspaces, CRAs) depending on their sensitivity to aircraft emissions (Niklaß et al., 2017b) were discussed. Niklaß et al. (2017a) investigate the cost-benefit potential of CRAs and compared them to climate-optimised trajectories similar to those in Grewe et al. (2014a) and Grewe et al. (2017b). They find similar potentials between both methods for summer flights but a large difference in winter where the CRAs become very large due to small gradients in the CCF data.

Here, we used CCF data provided by the REACT4C EU-project and developed aCCFs. A large amount of regressions between weather data as well as chemical data at the point and time of the emission and the CCFs are investigated and evaluated. The final aCCFs are based on potential vorticity, temperature, geopotential, and incoming solar radiation. The aCCFs represent the CCFs with different accuracy for the different emitted species. The water vapour impact is represented with the highest accuracy, whereas the NO_x emission effect on ozone has a lower accuracy. The spatial pattern generally agrees well, though the higher frequency variability is not well represented. However, there are uncertainties in calculating the original CCFs and it is not clear whether this high frequency variability is a real feature, i.e. based on physical processes or simply numerical noise. We show that the aCCFs are also in broad agreement with earlier climatological studies.

The aCCFs, presented here are limited to the North Atlantic region, since this is the modelling domain of the original REACT4C CCFs. However, since the meteorology is similar along a latitudinal band, we expect that the aCCFs are applicable in the whole northern extra-tropics. It remains open whether they can be extended to other regions. There are indications that, for example, the water vapour aCCF can be used globally. However, it remains to be proven. A further improvement of aCCFs could result from taking advantage of weather forecast data and basing the aCCFs approximation not only on the time of emission, but also taking into account a short-term weather forecast (Rosanka, 2017).

In general, the CCFs and aCCFs will always be affected by uncertainties from the modelling approach. However, we think that not including non-CO_2 effects in climate optimisation of aircraft trajectories leaves out a considerable part of aviation's climate impact, though there are significant uncertainties. The next steps, which are beyond the scope of this work, are to quantify these uncertainties based on an Earth System Model which includes an air traffic optimisation (Yamashita et al., 2016) and good diagnostics (Grewe et al., 2017c) and thereby verify the potential to reduce the climate impact by climate-optimised routing using aCCFs (Matthes et al.,

2017). First results indicate the feasibility of such an verification approach (Yin et al., 2018). Further work is required before such an approach can be used operationally and is described as a roadmap in Grewe et al. (2017b). This work is one of the first steps described in this roadmap.

Acknowledgements

CCF and model weather data were provided by the European Union FP7 Project REACT4C (Reducing Emissions from Aviation by Changing Trajectories for the benefit of Climate: http://www.react4c.eu/). The computational resources for calculating the CCFs were made available by the German Climate Computing Center (DKRZ) through support from the German Federal Ministry of Education and Research (BMBF) and by the Leibniz- Rechenzentrum (LRZ). The project ATM4E (Air Traffic Management for Environment: http://atm4e.eu/) has received funding from the SESAR Joint Undertaking under grant agreement No 699395 under European Union's Horizon 2020 research and innovation programme. We would like to thank Stephan Körner from DLR for providing an internal review.

Appendix A. Parameter overview of algorithms

Tables A.1,A.2,A.3,A.4,A.5,A.6,A.7,A.8,A.9,A.10,A.11,A.12.

Table A.1
Parameter overview for water vapour linear pressure and squared tropopause algorithm, Eq. (1).

	Units	Estimate	Std. Error	t value	$Pr(X > \|t\|)$
β_0	$\mathrm{K\,kg(fuel)^{-1}}$	3.72×10^{-16}	1.21×10^{-17}	3.09×10^{1}	1.47×10^{-158}
β_1	$\mathrm{K\,kg(fuel)^{-1}\,Pa^{-3}}$	2.05×10^{-28}	4.46×10^{-30}	4.59×10^{1}	1.59×10^{-277}

Table A.2
Parameter overview for water vapour quartic relative tropopause pressure algorithm, Eq. (2).

	Units	Estimate	Std. Error	t value	$Pr(X > \|t\|)$
A	$\mathrm{K\,kg(fuel)^{-1}}$	3.34×10^{-16}	2.81×10^{-17}	1.19×10^{1}	5.73×10^{-31}
B	$\mathrm{K\,kg(fuel)^{-1}\,Pa^{-4}}$	4.21×10^{4}	2.50×10^{3}	1.69×10^{1}	4.36×10^{-58}
C	Pa	2.29×10^{-34}	4.49×10^{-35}	5.11×10^{0}	3.79×10^{-7}

Table A.3
Parameter overview for water vapour linear potential vorticity algorithm, Eq. (3).

	Units	Estimate	Std. Error	t value	$Pr(X > \|t\|)$
β_0	$\mathrm{K\,kg(fuel)^{-1}}$	4.05×10^{-16}	1.20×10^{-17}	3.37×10^{1}	7.90×10^{-181}
β_1	$\mathrm{K\,kg(fuel)^{-1}\,PVU^{-1}}$	1.48×10^{-16}	3.40×10^{-18}	4.37×10^{1}	5.63×10^{-260}

Table A.4
Parameter overview for water vapour reciprocal specific humidity algorithm, Eq. (4).

	Units	Estimate	Std. Error	t value	$Pr(X > \|t\|)$
β_0	$\mathrm{K\,kg(fuel)^{-1}}$	3.94×10^{-16}	1.43×10^{-17}	2.76×10^{1}	4.32×10^{-133}
β_1	$\mathrm{K\,kg(fuel)^{-1}\,(kg\,kg^{-1})^{-1}}$	9.09×10^{-21}	2.56×10^{-22}	3.55×10^{1}	7.68×10^{-195}

Table A.5
Parameter overview for ozone linear specific humidity algorithm, Eq. (6). The p-value for β_0 is beyond double-precision floating point range.

	Units	Estimate	Std. Error	t value	$Pr(X > \|t\|)$
β_0	$\mathrm{K\,kg(NO_2)^{-1}}$	1.97×10^{-12}	2.50×10^{-14}	7.91×10^{1}	$<2.23 \times 10^{-308}$
β_1	$\mathrm{K\,kg(NO_2)^{-1}\,(kg\,kg^{-1})^{-1}}$	1.73×10^{-9}	9.44×10^{-11}	1.83×10^{1}	4.57×10^{-67}

Table A.6
Parameter overview for ozone bilinear temperature and geopotential algorithm, Eq. (7).

	Units	Estimate	Std. Error	t value	$Pr(X > \|t\|)$
β_0	$K\,kg(NO_2)^{-1}$	-5.20×10^{-11}	2.34×10^{-12}	-2.22×10^{1}	2.36×10^{-93}
β_1	$K\,kg(NO_2)^{-1}\,K^{-1}$	2.30×10^{-13}	1.04×10^{-14}	2.20×10^{1}	3.65×10^{-92}
β_2	$K\,kg(NO_2)^{-1}\,(m^2\,s^{-2})^{-1}$	4.85×10^{-16}	2.66×10^{-17}	1.82×10^{1}	2.46×10^{-66}
β_3	$K\,kg(NO_2)^{-1}\,(K\,m^2\,s^{-2})^{-1}$	-2.04×10^{-18}	1.20×10^{-19}	-1.70×10^{1}	1.03×10^{-58}

Table A.7
Parameter overview for ozone trilinear temperature, geopotential and specific humidity algorithm, Eq. (8).

	Units	Estimate	Std. Error	t value	$Pr(X > \|t\|)$
β_0	$K\,kg(NO_2)^{-1}$	-4.24×10^{-11}	2.75×10^{-12}	-1.54×10^{1}	2.33×10^{-49}
β_1	$K\,kg(NO_2)^{-1}\,K^{-1}$	1.86×10^{-13}	1.23×10^{-14}	1.52×10^{1}	3.26×10^{-48}
β_2	$K\,kg(NO_2)^{-1}\,(m^2\,s^{-2})^{-1}$	4.06×10^{-16}	2.89×10^{-17}	1.41×10^{1}	4.70×10^{-42}
β_3	$K\,kg(NO_2)^{-1}\,(kg\,kg^{-1})^{-1}$	8.55×10^{-10}	1.32×10^{-10}	6.46×10^{0}	1.48×10^{-10}
β_4	$K\,kg(NO_2)^{-1}\,(K\,m^2\,s^{-2})^{-1}$	-1.69×10^{-18}	1.30×10^{-19}	-1.30×10^{1}	1.27×10^{-36}

Table A.8
Parameter overview for ozone quadrilinear temperature, geopotential, specific humidity and solar irradiance algorithm, Eq. (9).

	Units	Estimate	Std. Error	t value	$Pr(X > \|t\|)$
β_0	$K\,kg(NO_2)^{-1}$	-3.97×10^{-11}	2.76×10^{-12}	-1.44×10^{1}	1.25×10^{-43}
β_1	$K\,kg(NO_2)^{-1}\,K^{-1}$	1.76×10^{-13}	1.23×10^{-14}	1.44×10^{1}	1.45×10^{-43}
β_2	$K\,kg(NO_2)^{-1}\,(m^2\,s^{-2})^{-1}$	4.01×10^{-16}	2.86×10^{-17}	1.40×10^{1}	8.16×10^{-42}
β_3	$K\,kg(NO_2)^{-1}\,(kg\,kg^{-1})^{-1}$	9.24×10^{-10}	1.32×10^{-10}	7.03×10^{0}	3.39×10^{-12}
β_4	$K\,kg(NO_2)^{-1}\,(W\,m^{-2})^{-1}$	3.26×10^{-16}	5.86×10^{-17}	5.57×10^{0}	3.11×10^{-8}
β_5	$K\,kg(NO_2)^{-1}\,(K\,m^2\,s^{-2})^{-1}$	-1.70×10^{-18}	1.29×10^{-19}	-1.32×10^{1}	1.91×10^{-37}

Table A.9
Parameter overview for methane constant algorithm, Eq. (11). The p-value for β_0 is beyond double-precision floating point range.

	Units	Estimate	Std. Error	t value	$Pr(X > \|t\|)$
β_0	$K\,kg(NO_2)^{-1}$	-8.21×10^{-13}	6.36×10^{-15}	-1.29×10^{2}	$<2.23 \times 10^{-308}$

Table A.10
Parameter overview for methane linear geopotential algorithm, Eq. (12).

	Units	Estimate	Std. Error	t value	$Pr(X > \|t\|)$
β_0	$K\,kg(NO_2)^{-1}$	-1.30×10^{-12}	3.37×10^{-14}	-3.85×10^{1}	5.59×10^{-219}
β_1	$K\,kg(NO_2)^{-1}\,(m^2\,s^{-2})^{-1}$	5.06×10^{-18}	3.54×10^{-19}	1.43×10^{1}	2.60×10^{-43}

Table A.11
Parameter overview for methane bilinear geopotential and solar irradiance algorithm, Eq. (13).

	Units	Estimate	Std. Error	t value	$Pr(X > \|t\|)$
β_0	$K\,kg(NO_2)^{-1}$	-9.83×10^{-13}	5.41×10^{-14}	-1.82×10^{1}	3.18×10^{-66}
β_1	$K\,kg(NO_2)^{-1}\,(m^2\,s^{-2})^{-1}$	1.99×10^{-18}	5.85×10^{-19}	3.40×10^{0}	6.91×10^{-4}
β_2	$K\,kg(NO_2)^{-1}\,(W\,m^{-2})^{-1}$	-6.32×10^{-16}	8.25×10^{-17}	-7.66×10^{0}	3.59×10^{-14}
β_3	$K\,kg(NO_2)^{-1}\,(W\,m^{-2}\,m^2\,s^{-2})^{-1}$	6.12×10^{-21}	8.68×10^{-22}	7.05×10^{0}	2.88×10^{-12}

Table A.12
Parameter overview for methane bilinear ozone and potential temperature algorithm, Eq. (14).

	Units	Estimate	Std. Error	t value	$Pr(X > \|t\|)$
β_0	$K\,kg(NO_2)^{-1}$	-2.81×10^{-12}	1.31×10^{-13}	-2.15×10^{1}	3.31×10^{-88}
β_1	–	-1.36×10^{-1}	6.37×10^{-3}	-2.14×10^{1}	1.96×10^{-87}
β_2	$K\,kg(NO_2)^{-1}\,K^{-1}$	7.11×10^{-15}	4.19×10^{-16}	1.69×10^{1}	1.57×10^{-58}

Appendix B. Calculation of solar irradiance

The solar irradiance F_{in} used in the methane aCCF is given by:

$$F_{in} = S \times \cos\theta \tag{B.1}$$

$$\theta = \sin\phi \times \sin\delta + \cos\phi \times \cos\delta \tag{B.2}$$

$$\delta = -23.44 \times \cos(360/365 \times [N + 10]), \tag{B.3}$$

where S is the solar constant, δ the declination, ϕ the latitude, and N the day of the year.

Appendix C. Supplementary material

Supplementary data associated with this article can be found, in the online version, at https://doi.org/10.1016/j.trd.2018.12.016.

References

Berntsen, T.K., Isaksen, I.S.A., 1999. Effects of lightning and convection on changes in tropospheric ozone due to NO_x emissions from aircraft. Tellus B 51, 766–788. https://doi.org/10.1034/j.1600-0889.1999.t01-3-00003.x.

Derwent, R.G., Collins, W.J., Johnson, C.E., Stevenson, D.S., 2001. Transient behaviour of tropospheric ozone precursors in a global 3-d ctm and their indirect greenhouse effects. Clim. Change 49, 463–487. https://doi.org/10.1023/A:1010648913655.

Dietmüller, S., Jöckel, P., Tost, H., Kunze, M., Gellhorn, C., Brinkop, S., Frömming, C., Ponater, M., Steil, B., Lauer, A., Hendricks, J., 2016. A new radiation infrastructure for the modular earth submodel system (MESSy, based on version 2.51). Geosci. Model Dev. 9, 2209–2222. https://doi.org/10.5194/gmd-9-2209-2016.

Frömming, C., Grewe, V., Matthes, S., Brinkop, S., Haslerud, A.S., Irvine, E.A., Rosanka, S., van Manen, J., 2019. Inuence of weather situation on aviation emission effects: The REACT4C climate change functions (in preparation).

Frömming, C., Ponater, M., Dahlmann, K., Grewe, V., Lee, D.S., Sausen, R., 2012. Aviation-induced radiative forcing and surface temperature change in dependency of the emission altitude. J. Geophys. Res.: Atmosph. 117. https://doi.org/10.1029/2012JD018204. d19104.

Fuglestvedt, J.S., Shine, K.P., Berntsen, T., Cook, J., Lee, D.S., Stenke, A., Skeie, R.B., Velders, G.J.M., Waitz, I.A., 2010. Transport impacts on atmosphere and climate: metrics. Atmosph. Environ. 44, 4648–4677. https://doi.org/10.1016/j.atmosenv.2009.04.044. Transport Impacts on Atmosphere and Climate: The ATTICA Assessment Report.

Gauss, M., Isaksen, I.S.A., Lee, D.S., Søvde, O.A., 2006. Impact of aircraft NO_x emissions on the atmosphere - tradeoffs to reduce the impact. Atmosph. Chem. Phys. 6, 1529–1548. https://doi.org/10.5194/acp-6-1529-2006.

Grewe, V., 2013. A generalized tagging method. Geosci. Model Dev. 6, 247–253. https://doi.org/10.5194/gmd-6-247-2013.

Grewe, V., Champougny, T., Matthes, S., Frömming, C., Brinkop, S., Søvde, O.A., Irvine, E.A., Halscheidt, L., 2014a. Reduction of the air traffic's contribution to climate change: a REACT4C case study. Atmosph. Environ. 94, 616–625. https://doi.org/10.1016/j.atmosenv.2014.05.059.

Grewe, V., Dahlmann, K., 2015. How ambiguous are climate metrics? And are we prepared to assess and compare the climate impact of new air traffic technologies? Atmosph. Environ. 106, 373–374. https://doi.org/10.1016/j.atmosenv.2015.02.039.

Grewe, V., Dahlmann, K., Flink, J., Frmming, C., Ghosh, R., Gierens, K., Heller, R., Hendricks, J., Jckel, P., Kaufmann, S., Klker, K., Linke, F., Luchkova, T., Lhrs, B., Van Manen, J., Matthes, S., Minikin, A., Nikla, M., Plohr, M., Righi, M., Rosanka, S., Schmitt, A., Schumann, U., Terekhov, I., Unterstrasser, S., Vzquez-Navarro, M., Voigt, C., Wicke, K., Yamashita, H., Zahn, A., Ziereis, H., 2017a. Mitigating the climate impact from aviation: achievements and results of the dlr wecare project. Aerospace, 4 doi:https://doi.org/10.3390/aerospace4030034.

Grewe, V., Dameris, M., Fichter, C., Sausen, R., 2002. Impact of aircraft NO_x emissions. Part 1: Interactively coupled climate-chemistry simulations and sensitivities to climate-chemistry feedback, lightning and model resolution. Meteorol. Z. 11, 177–186. https://doi.org/10.1127/0941-2948/2002/0011-0177.

Grewe, V., Frömming, C., Matthes, S., Brinkop, S., Ponater, M., Dietmüller, S., Jöckel, P., Garny, H., Tsati, E., Dahlmann, K., Søvde, O.A., Fuglestvedt, J., Berntsen, T.K., Shine, K.P., Irvine, E.A., Champougny, T., Hullah, P., 2014b. Aircraft routing with minimal climate impact: the REACT4C climate cost function modelling approach (v1.0). Geosci. Model Dev. 7, 175–201. https://doi.org/10.5194/gmd-7-175-2014.

Grewe, V., Linke, F., 2017. Eco-efficiency in aviation. Meteorol. Z. 26, 689–696. https://doi.org/10.1127/metz/2017/0762.

Grewe, V., Matthes, S., Frömming, C., Brinkop, S., Jöckel, P., Gierens, K., Champougny, T., Fuglestvedt, J., Haslerud, A., Irvine, E., Shine, K., 2017b. Feasibility of climate-optimized air traffic routing for trans-atlantic flights. Environ. Res. Lett. 12, 034003. https://doi.org/10.1088/1748-9326/aa5ba0.

Grewe, V., Stenke, A., 2008. AirClim: an efficient tool for climate evaluation of aircraft technology. Atmosph. Chem. Phys. 8, 4621–4639. https://doi.org/10.5194/acp-8-4621-2008.

Grewe, V., Tsati, E., Mertens, M., Frömming, C., Jöckel, P., 2017c. Contribution of emissions to concentrations: the TAGGING 1.0 submodel based on the modular earth submodel system (MESSy 2.52). Geosci. Model Dev. 10, 2615–2633. https://doi.org/10.5194/gmd-10-2615-2017.

Hartjes, S., Hendriks, T., Visser, H.G., 2016. Contrail mitigation through 3D aircraft trajectory optimization. In: 16th AIAA Aviation Technology, Integration, and Operations Conference, American Institute of Aeronautics and Astronautics. doi:https://doi.org/10.2514/6.2016-3908.

Holmes, C.D., Prather, M.J., Søvde, O.A., Myhre, G., 2013. Future methane, hydroxyl, and their uncertainties: key climate and emission parameters for future predictions. Atmosph. Chem. Phys. 13, 285–302. https://doi.org/10.5194/acp-13-285-2013.

Holmes, C.D., Tang, Q., Prather, M.J., 2011. Uncertainties in climate assessment for the case of aviation NO. Proc. Natl. Acad. Sci. 108, 10997–11002. https://doi.org/10.1073/pnas.1101458108.

Irvine, E.A., Hoskins, B.J., Shine, K.P., Lunnon, R.W., Frömming, C., 2013. Characterizing North Atlantic weather patterns for climate-optimal aircraft routing. Meteorol. Appl. 20, 80–93. https://doi.org/10.1002/met.1291.

Jöckel, P., Kerkweg, A., Pozzer, A., Sander, R., Tost, H., Riede, H., Baumgaertner, A., Gromov, S., Kern, B., 2010. Development cycle 2 of the modular earth submodel system (MESSy2). Geosci. Model Dev. 3, 717–752. https://doi.org/10.5194/gmd-3-717-2010.

Jöckel, P., Tost, H., Pozzer, A., Kunze, M., Kirner, O., Brenninkmeijer, C.A.M., Brinkop, S., Cai, D.S., Dyroff, C., Eckstein, J., Frank, F., Garny, H., Gottschaldt, K.D., Graf, P., Grewe, V., Kerkweg, A., Kern, B., Matthes, S., Mertens, M., Meul, S., Neumaier, M., Nützel, M., Oberländer-Hayn, S., Ruhnke, R., Runde, T., Sander, R., Scharffe, D., Zahn, A., 2016. Earth system chemistry integrated modelling (ESCiMo) with the modular earth submodel system (MESSy) version 2.51. Geosci. Model Dev. 9, 1153–1200. https://doi.org/10.5194/gmd-9-1153-2016.

Köhler, M.O., Rädel, G., Dessens, O., Shine, K.P., Rogers, H.L., Wild, O., Pyle, J.A., 2008. Impact of perturbations to nitrogen oxide emissions from global aviation. J. Geophys. Res.: Atmosph. 113 (d11), 305. https://doi.org/10.1029/2007JD009140.

Köhler, M.O., Rädel, G., Shine, K.P., Rogers, H.L., Pyle, J.A., 2013. Latitudinal variation of the effect of aviation NO_x emissions on atmospheric ozone and methane and related climate metrics. Atmosph. Environ. 64, 1–9. https://doi.org/10.1016/j.atmosenv.2012.09.013.

Lee, D.S., Fahey, D.W., Forster, P.M., Newton, P.J., Wit, R.C., Lim, L.L., Owen, B., Sausen, R., 2009. Aviation and global climate change in the 21st century. Atmosph. Environ. 43, 3520–3537. https://doi.org/10.1016/j.atmosenv.2009.04.024.

Lee, D.S., Pitari, G., Grewe, V., Gierens, K., Penner, J.E., Petzold, A., Prather, M., Schumann, U., Bais, A., Berntsen, T., Iachetti, D., Lim, L.L., Sausen, R., 2010. Transport impacts on atmosphere and climate: Aviation. Atmosph. Environ. 44, 4678–4734. https://doi.org/10.1016/j.atmosenv.2009.06.005. Transport Impacts on Atmosphere and Climate: The ATTICA Assessment Report.

Mahashabde, A., Wolfe, P., Ashok, A., Dorbian, C., He, Q., Fan, A., Lukachko, S., Mozdzanowska, A., Wollersheim, C., Barrett, S.R., Locke, M., Waitz, I.A., 2011. Assessing the environmental impacts of aircraft noise and emissions. Prog. Aerospace Sci. 47, 15–52. https://doi.org/10.1016/j.paerosci.2010.04.003.

van Manen, J., 2017. Aviation H_2O and NO_x climate cost functions based on local weather. Master's thesis. Delft University of Technology. < http://resolver.tudelft.nl/uuid:597ed925-9e3b-4300-a2c2-84c8cc97b5b7 > .

Matthes, S., Grewe, V., Dahlmann, K., Frömming, C., Irvine, E., Lim, L., Linke, F., Lührs, B., Owen, B., Shine, K., Stromatas, S., Yamashita, H., Yin, F., 2017. A concept for multi-criteria environmental assessment of aircraft trajectories. Aerospace 4. https://doi.org/10.3390/aerospace4030042.

Myhre, G., Nilsen, J.S., Gulstad, L., Shine, K.P., Rognerud, B., Isaksen, I.S.A., 2007. Radiative forcing due to stratospheric water vapour from CH_4 oxidation. Geophys. Res. Lett. 34, l01807. https://doi.org/10.1029/2006GL027472.

Myhre, G., Shindell, D., Bréon, F.M., Collins, W., Fuglestvedt, J., Huang, J., Koch, D., Lamarque, J.F., Lee, D., Mendoza, B., Nakajima, T., Robock, A., Stephens, G., Takemura, T., Zhang, H., 2013. Anthropogenic and natural radiative forcing, in: Stocker, T.F., Qin, D., Plattner, G.K., Tignor, M., Allen, S.K., Boschung, J., Nauels, A., Xia, Y., Bex, V., Midgley, P.M. (Eds.), Climate Change 2013: The Physical Science Basis. Contribution of Working Group I to the Fifth Assessment Report of the Intergovernmental Panel on Climate Change. Cambridge University Press, Cambridge, United Kingdom and New York, NY, USA (Chapter 8).

Niklaß, M., Gollnick, V., Lührs, B., Dahlmann, K., Frömming, C., Grewe, V., van Manen, J., 2017a. Cost-benefit assessment of climate-restricted airspaces as an interim climate mitigation option. J. Air Transport. 25. https://doi.org/10.2514/1.D0045.

Niklaß, M., Lührs, B., Grewe, V., Dahlmann, K., Luchkova, T., Linke, F., Gollnick, V., 2017b. Potential to reduce the climate impact of aviation by climate restricted airspaces. Transport Policy. https://doi.org/10.1016/j.tranpol.2016.12.010. in press.

Penner, J.E., Lister, D.H., Griggs, D.J., Dokken, D.J., McFarland, M., 1999. Aviation and the Global Atmosphere: A Special Report of IPCC Working Groups I and III in Collaboration with the Scientific Assessment Panel to the Montreal Protocol on Substances that Deplete the Ozone Layer. Cambridge University Press, UK.

Pitari, G., Cionni, I., Di Genova, G., Søvde, O.A., Lim, L., 2017. Radiative forcing from aircraft emissions of NO_x: model calculations with CH_4 surface flux boundary condition. Meteorol. Z. 26, 663–687. https://doi.org/10.1127/metz/2016/0776.

Roeckner, E., Bäuml, G., Bonaventura, L., Brokopf, R., Esch, M., Giorgetta, M., Hagemann, S., Kirchner, I., Kornblueh, L., Manzini, E., Rhodin, A., Schlese, U., Schulzweida, U., Tompkins, A., 2003. The Atmospheric General Circulation Model ECHAM5. Part I: Model Description. Technical Report 354. Max-Planck-Institut für Meteorologie.

Roeckner, E., Brokopf, R., Esch, M., Giorgetta, M., Hagemann, S., Kornblueh, L., Manzini, E., Schlese, U., Schulzweida, U., 2006. Sensitivity of simulated climate to horizontal and vertical resolution in the ECHAM5 atmosphere model. J. Clim. 19, 3771–3791. https://doi.org/10.1175/JCLI3824.1.

Rosanka, S.H., 2017. Weather influence on aviation NO_x climate impacts via ozone and methane. Master's thesis. Delft University of Technology. < http://resolver.tudelft.nl/uuid:3a8c9694-45ce-426d-bc59-75e4398cdd09 > .

Rosenow, J., Lindner, M., Fricke, H., 2017. Impact of climate costs on airline network and trajectory optimization: a parametric study. CEAS Aeronaut. J. 8, 371–384. https://doi.org/10.1007/s13272-017-0239-2.

Sander, R., Baumgaertner, A., Gromov, S., Harder, H., Jöckel, P., Kerkweg, A., Kubistin, D., Regelin, E., Riede, H., Sandu, A., Taraborrelli, D., Tost, H., Xie, Z.Q., 2011. The atmospheric chemistry box model CAABA/MECCA-3.0. Geosci. Model Dev. 4, 373–380. https://doi.org/10.5194/gmd-4-373-2011.

Schumann, U., Graf, K., Mannstein, H., 2011. Potential to reduce the climate impact of aviation by ight level changes. In: 3rd AIAA Atmospheric Space Environments Conference. AIAA paper 2011-3376.

Skowron, A., Lee, D., Len, R.D., 2013. The assessment of the impact of aviation NO_x on ozone and other radiative forcing responses the importance of representing cruise altitudes accurately. Atmosph. Environ. 74, 159–168. https://doi.org/10.1016/j.atmosenv.2013.03.034.

Sridhar, B., Chen, N.Y., Ng, H.K., 2013. Energy efficient contrail mitigation strategies for reducing the environmental impact of aviation. In: Tenth USA/Europe Air Traffic Management Research and Development Seminar. < http://www.atmseminar.org/seminarContent/seminar10/papers/212-Sridhar_0125130119-Final-Paper-4-9-13.pdf > .

Stevenson, D.S., Derwent, R.G., 2009. Does the location of aircraft nitrogen oxide emissions affect their climate impact? Geophys. Res. Lett. 36, 00. https://doi.org/10.1029/2009GL039422.l17810.

Stevenson, D.S., Doherty, R.M., Sanderson, M.G., Collins, W.J., Johnson, C.E., Derwent, R.G., 2004. Radiative forcing from aircraft NO_x emissions: mechanisms and seasonal dependence. J. Geophys. Res.: Atmosph. 109. https://doi.org/10.1029/2004JD004759.d17307.

Wilcox, L.J., Shine, K.P., Hoskins, B.J., 2012. Radiative forcing due to aviation water vapour emissions. Atmosph. Environ. 63, 1–13. https://doi.org/10.1016/j.atmosenv.2012.08.072.

Wild, O., Prather, M.J., Akimoto, H., 2001. Indirect long-term global radiative cooling from nox emissions. Geophys. Res. Lett. 28, 1719–1722. https://doi.org/10.1029/2000GL012573.

Yamashita, H., Grewe, V., Jöckel, P., Linke, F., Schaefer, M., Sasaki, D., 2016. Air traffic simulation in chemistry-climate model EMAC 2.41: AirTraf 1.0. Geosci. Model Dev. 9, 3363–3392. https://doi.org/10.5194/gmd-9-3363-2016.

Yin, F., Grewe, V., van Manen, J., Matthes, S., Yamashita, H., Linke, F., Lührs, B., 2018. Verification of the ozone algorithmic climate change functions for predicting the short-term NO_x effects from aviation en-route. In: International Conference on Research in Air Transportation (ICRAT).

Zou, B., Buxi, G.S., Hansen, M., 2016. Optimal 4D aircraft trajectories in a contrail-sensitive environment. Networks Spat. Econ. 16, 415–446. https://doi.org/10.1007/s11067-013-9210-x.